

# Experimental measurement of the complete quantum geometry of a solid-state spin system

Min Yu,<sup>1,2,\*</sup> Pengcheng Yang,<sup>1,2,\*</sup> Musang Gong,<sup>1,2</sup> Qingyun Cao,<sup>3,1,2</sup> Qiuyu Lu,<sup>1,2</sup> Haibin Liu,<sup>1,2</sup> Martin B. Plenio,<sup>4,2</sup> Fedor Jelezko,<sup>3,2</sup> Tomoki Ozawa,<sup>5</sup> Nathan Goldman,<sup>6</sup> Shaoliang Zhang,<sup>1,2,†</sup> and Jianming Cai<sup>1,2,‡</sup>

<sup>1</sup>*School of Physics, Huazhong University of Science and Technology, Wuhan 430074, China*

<sup>2</sup>*International Joint Laboratory on Quantum Sensing and Quantum Metrology, Huazhong University of Science and Technology, Wuhan 430074, China*

<sup>3</sup>*Institut für Quantenoptik & IQST, Albert-Einstein Allee 11, Universität Ulm, D-89081 Ulm, Germany*

<sup>4</sup>*Institut für Theoretische Physik & IQST, Albert-Einstein Allee 11, Universität Ulm, D-89081 Ulm, Germany*

<sup>5</sup>*Interdisciplinary Theoretical and Mathematical Sciences Program (iTHEMS), RIKEN, Wako, Saitama 351-0198, Japan*

<sup>6</sup>*Center for Nonlinear Phenomena and Complex Systems, Université Libre de Bruxelles, CP 231, Campus Plaine, B-1050 Brussels, Belgium*

(Dated: December 15, 2024)

Geometry and topology are fundamental concepts, which underlie a wide range of fascinating physical phenomena such as topological states of matter and topological defects. In quantum mechanics, the geometry of quantum states is fully captured by the quantum geometric tensor. Using a solid-state spin system, we demonstrate a strong connection between coherent Rabi oscillations upon parametric modulations and the geometry of the underlying quantum states. We exploit this useful relation to perform, for the first time, an experimental measurement of the complete quantum geometric tensor. Our results establish coherent dynamical responses as a versatile probe for quantum geometry, and they pave the way for the detection of topological phenomena in solid state.

The quantum geometric tensor (QGT) constitutes a central and ubiquitous concept in quantum mechanics, by providing a geometric structure to the Hilbert space [1–5]. The imaginary part of this tensor corresponds to the well-known Berry curvature [6, 7], which acts as an effective “electromagnetic” tensor in parameter space [8]. This geometric quantity, which is formally associated with the parallel transport of wave functions, is responsible for striking observable phenomena such as the geometric phase [8], the anomalous Hall effect [9], and topological states of matter [10]. In contrast, the real part of the QGT constitutes the Fubini-Study metric [2, 3, 5], which defines a notion of distance (a Riemannian metric) in parameter space through the overlap of wavefunctions. This “quantum metric” was shown to play an important role in various contexts, including quantum phase transitions [11], open quantum systems [12], orbital magnetism [13, 14], localization in insulators [15], excitonic Lamb-shifts in transition-metal dichalcogenides [16], superfluidity in flat bands [17], and topological matter [18, 19]. Various manifestations of the QGT have been observed in experiments, using very different physical platforms and probes. On the one hand, the local Berry curvature has been detected in ultracold atomic gases [20–22], coupled optical fibers [23], and solids [24, 25]. On the other hand, a first manifestation of the quantum metric – the so-called Wannier-spread functional of Bloch bands [26] – was recently measured in cold atoms [27, 28]. Nevertheless, a direct measurement of the complete QGT is still lacking.

Here, we report on the first experimental measurement of the complete QGT, using an NV-center spin in diamond. Following the proposal of Ref. [28], we exploit the relation between the QGT and the response of quantum systems upon parametric modulations in order to map out the full Fubini-Study metric as well as the local Berry curvature. Our results do not only enforce the deep connections between out-of-equilibrium

dynamics and quantum geometry [29–37], but they also reveal a universal tool for the detection of geometric and topological properties in quantum systems.

We consider the general Hamiltonian  $\mathcal{H}(\boldsymbol{\lambda})$  of a discrete quantum system, which depends on a set of dimensionless parameters  $\boldsymbol{\lambda} = (\lambda_1, \lambda_2, \dots, \lambda_N)$ , where  $N$  is the dimension of parameter space. The eigenstates and eigenvalues of the Hamiltonian are defined via

$$\mathcal{H}(\boldsymbol{\lambda})|n(\boldsymbol{\lambda})\rangle = \epsilon_n(\boldsymbol{\lambda})|n(\boldsymbol{\lambda})\rangle. \quad (1)$$

If the Hamiltonian has no energy degeneracy, the QGT associated with the eigenstate  $|n(\boldsymbol{\lambda})\rangle$  is defined as [5]

$$\chi_{\mu\nu}^{(n)} = \langle \partial_\mu n(\boldsymbol{\lambda}) | (1 - |n(\boldsymbol{\lambda})\rangle\langle n(\boldsymbol{\lambda})|) | \partial_\nu n(\boldsymbol{\lambda}) \rangle. \quad (2)$$

The real part  $\text{Re}(\chi_{\mu\nu}) = g_{\mu\nu}$  is the Fubini-Study metric that defines the distance between nearby states  $|\psi_n(\boldsymbol{\lambda})\rangle$  and  $|\psi_n(\boldsymbol{\lambda} + d\boldsymbol{\lambda})\rangle$  in parameter space, while the imaginary part  $\text{Im}(\chi_{\mu\nu}) = -\mathcal{F}_{\mu\nu}(\boldsymbol{\lambda})/2$  is related to the Berry curvature  $\mathcal{F}_{\mu\nu}(\boldsymbol{\lambda})$ . It is useful to express the QGT in the form

$$\chi_{\mu\nu}^{(n)} = \sum_{m \neq n} \frac{\langle n(\boldsymbol{\lambda}) | \partial_\mu \mathcal{H}(\boldsymbol{\lambda}) | m(\boldsymbol{\lambda}) \rangle \langle m(\boldsymbol{\lambda}) | \partial_\nu \mathcal{H}(\boldsymbol{\lambda}) | n(\boldsymbol{\lambda}) \rangle}{(\epsilon_m(\boldsymbol{\lambda}) - \epsilon_n(\boldsymbol{\lambda}))^2}, \quad (3)$$

so as to highlight the relation between this geometric quantity and the coupling matrix elements (Rabi frequencies) connecting eigenstates  $|n(\boldsymbol{\lambda})\rangle$  and  $|m(\boldsymbol{\lambda})\rangle$  upon a parametric modulation (see Refs. [28, 38] and below)

$$\Omega_{n \leftrightarrow m}(\boldsymbol{\lambda}) \propto \langle m(\boldsymbol{\lambda}) | \partial_\mu \mathcal{H}(\boldsymbol{\lambda}) | n(\boldsymbol{\lambda}) \rangle. \quad (4)$$

In our experiment, we perform a full quantum-geometric measurement of a generic two-level system, which is described

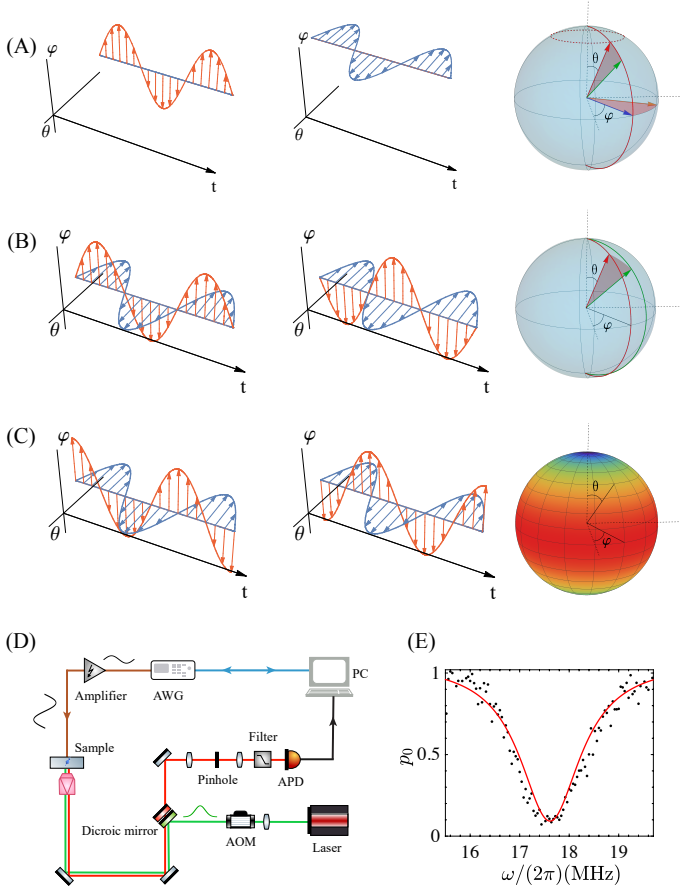


**FIG. 1. Probing quantum geometry from coherent response on parametric modulation.** (A-C) show different types of parametric modulation  $(\theta_t, \varphi_t)$ , including (A-B) linear parametric modulation  $\theta_t = \theta_0 + a_\theta \sin(\omega t)$ ,  $\varphi_t = \varphi_0 + a_\varphi \sin(\omega t)$  for the measurement of the diagonal [off-diagonal] element of the Fubini-Study metric with  $a_\theta = 0$  or  $a_\varphi = 0$  (A) [ $a_\theta = \pm a_\varphi \neq 0$ ] (B); (C) elliptical parametric modulation for the measurement of the local Berry curvature (as indicated by color map) with  $\theta_t = \theta_0 + a_\theta \sin(\omega t)$  and  $\varphi_t = \varphi_0 \pm a_\varphi \cos(\omega t)$ . (D) The sketch of experiment setup for quantum geometric measurement using the NV center spin in diamond. A green laser pulse polarises the NV center spin into the  $|m_s = 0\rangle$  state. The engineered microwave from an arbitrary waveform generator (Tektronix AWG 70002A, 16GS/s) is amplified before being delivered to the sample and coherently drives the NV center spin. The NV center spin state is detected by an APD via spin-dependent fluorescence. (E) An example of parametric modulation resonance measurement. The probability that the NV center spin remains in the initial eigenstate at time  $T = 400$  ns as a function of the modulation frequency  $\omega$  of linear parametric modulation  $\theta_t = \theta_0 + a_\theta \sin(\omega t)$  and  $\varphi_t = \varphi_0$  with  $(\theta_0, \varphi_0) = (5\pi/6, 0)$  and  $a_\theta = 0.1$ .

by the following Hamiltonian

$$\mathcal{H}(\theta, \varphi) = \frac{A}{2} \begin{pmatrix} \cos \theta & \sin \theta e^{-i\varphi} \\ \sin \theta e^{i\varphi} & -\cos \theta \end{pmatrix}, \quad (5)$$

where  $(\theta, \varphi)$  form the parameter space. In such a system, the non-zero elements of the QGT related to the low-energy state

are

$$g_{\theta\theta} = 1/4, \quad g_{\varphi\varphi} = \sin^2 \theta/4, \quad g_{\theta\varphi} = 0, \quad \mathcal{F}_{\theta\varphi} = \sin \theta/2. \quad (6)$$

These components fully characterize the underlying geometry: the quantum metric  $g$  corresponds to the natural metric of a sphere  $S^2$ , embedded in  $\mathbb{R}^3$  with fixed radius  $R = 1/2$ , while the Berry curvature  $\mathcal{F}_{\theta\varphi}$  corresponds to the “magnetic” field of a fictitious Dirac monopole located at the center of that sphere [19].

As mentioned earlier, the components of the QGT can be directly connected to the frequency of a Rabi oscillation upon parametric modulation. We consider two types of parametric modulations [28]: (a) a “linear” parametric modulation with  $\theta_t = \theta_0 + a_\theta \sin(\omega t)$ ,  $\varphi_t = \varphi_0 + a_\varphi \sin(\omega t)$ ; (b) an “elliptical” parametric modulation with  $\theta_t = \theta_0 + a_\theta \sin(\omega t)$ ,  $\varphi_t = \varphi_0 + a_\varphi \cos(\omega t)$ ; see Fig. 1. Setting  $a_\theta, a_\varphi \ll 1$ , the time-dependent Hamiltonian can be expressed as

$$\begin{aligned} \mathcal{H}(\theta_t, \varphi_t) \cong & \mathcal{H}(\theta_0, \varphi_0) + a_\theta (\partial_\theta \mathcal{H}) \sin(\omega t) \\ & + a_\varphi (\partial_\varphi \mathcal{H}) \sin(\omega t) : \text{linear} \\ & + a_\varphi (\partial_\varphi \mathcal{H}) \cos(\omega t) : \text{elliptical}. \end{aligned} \quad (7)$$

Setting the modulation frequency  $\omega_{g \leftrightarrow e}$  on resonance generates a coherent transition between the eigenstates, the Rabi frequency of which allows one to measure the QGT [28, 38]; see Eqs.(3-4).

In our experiment, the two-level system in Eq. (5) is obtained from a single nitrogen-vacancy (NV) center in an electronic grade diamond. The NV center spin has a triplet ground state manifold with three spin sublevels  $m_s = 0, \pm 1$ . We apply a magnetic field  $B_z = 509$  G along the NV axis to lift the degeneracy of  $m_s = \pm 1$ . The associated nitrogen nuclear spin of NV center is polarised when the NV centre is initialised by a 532 nm green laser pulse. A two-level system is supported by the spin sublevels  $m_s = 0$  and  $m_s = -1$ , which have an energy splitting  $\omega_0 = D - \gamma B_z$ ; the zero field splitting is  $D = (2\pi)2.87$  GHz and  $\gamma$  is the electron gyromagnetic ratio.

The experimental setup is sketched in Fig. 1(D). We first prepare the system in the eigenstate of the Hamiltonian  $\mathcal{H}(\theta_0, \varphi_0)$ , i.e.  $|n(\theta_0, \varphi_0)\rangle = \cos \frac{\theta_0}{2} |-1\rangle + \sin \frac{\theta_0}{2} e^{i\varphi_0} |0\rangle$ . This is achieved by first applying a 532 nm green laser pulse to initialise the NV center spin in the  $m_s = 0$  state. A subsequent microwave pulse  $\mathcal{H}_i(t) = \Omega \sin(\omega_0 t + \varphi_0) \sigma_x$ , applied over a duration  $t_{\theta_0} = \theta_0/\Omega$ , rotates the NV center spin around the axis  $\hat{n}(\varphi_0) = (\cos \varphi_0, \sin \varphi_0, 0)$  by an angle  $\theta_0$ . The initial state preparation is verified by a spin-locking type experiment, which confirms that the NV spin is prepared in the eigenstate of  $\mathcal{H}(\theta_0, \varphi_0)$  [38]. The microwave is generated using an arbitrary waveform generator (AWG), and is delivered to the NV center in the sample through a copper microwave antenna, after being amplified by a microwave amplifier [Fig. 1(D)].

The precise control over the AWG, in both amplitude and timing, allows us to engineer the microwave driving field with accurate amplitude and phase modulation. This leads to the

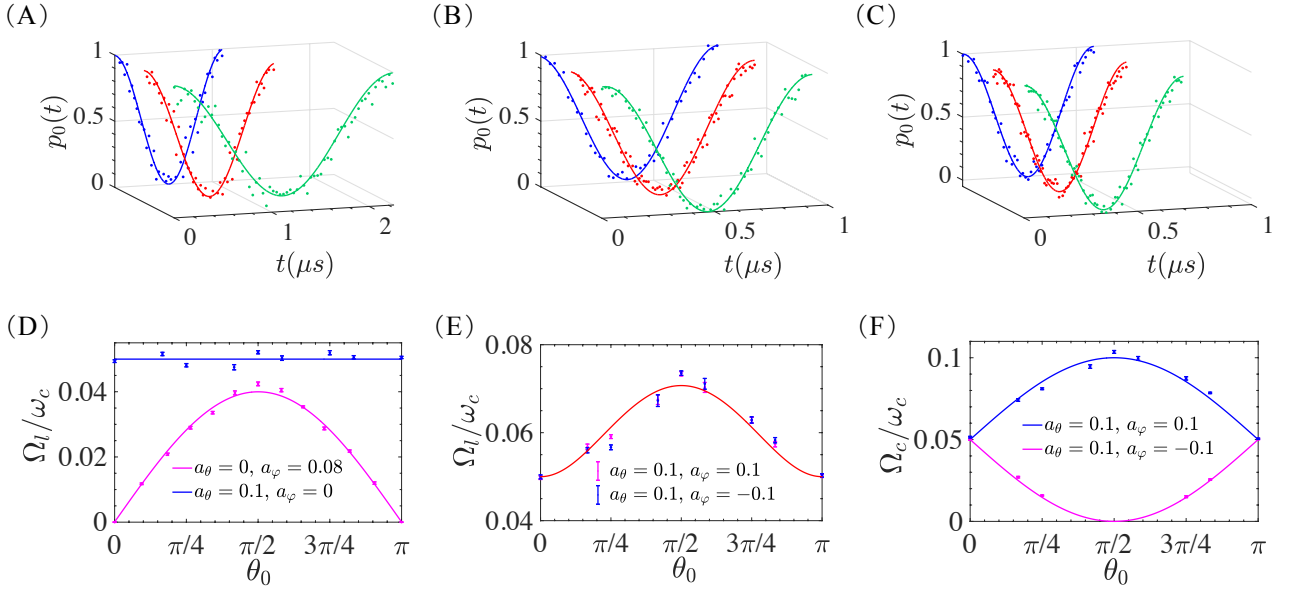


FIG. 2. **Parametric modulation induced coherent excitation.** (A-B) Resonance oscillation under linear parametric modulation with  $a_\theta = 0$ ,  $a_\varphi = 0.08$  (A) and  $a_\theta = 0.1$ ,  $a_\varphi = 0.1$  (B). (C) Resonance oscillation under elliptical parametric modulation with  $a_\theta = 0.1$ ,  $a_\varphi = 0.1$ . The other experimental parameters are: (A)  $\omega_c = (2\pi)20.98$  MHz ( $\theta_0 = \pi/6$ , green),  $(2\pi)21.61$  MHz ( $\theta_0 = \pi/3$ , red),  $(2\pi)20.73$  MHz ( $\theta_0 = \pi/2$ , blue); (B)  $\omega_c = (2\pi)19.11$  MHz ( $\theta_0 = \pi/6$ , green),  $(2\pi)17.8$  MHz ( $\theta_0 = 5\pi/12$ , red),  $(2\pi)16.72$  MHz ( $\theta_0 = \pi/2$ , blue); (C)  $\omega_c = (2\pi)19.11$  MHz ( $\theta_0 = \pi/6$ , green),  $(2\pi)17.8$  MHz ( $\theta_0 = 5\pi/12$ , red),  $(2\pi)16.72$  MHz ( $\theta_0 = \pi/2$ , blue). (D-F) Rabi frequency of parametric modulation induced resonant coherent transition (in the unit of resonant frequency  $\omega_c$ ) as a function of the parameter  $\theta_0$  for linear (D-E) and elliptical (F) parametric modulation. The curves represent the corresponding values from theoretical predictions. In (A-F), we set the parameter  $\varphi_0 = 0$ .

implementation of the generic two-level system

$$\mathcal{H}(t) = \frac{\omega_0}{2}\sigma_z + \mathcal{V}(t)\sigma_x, \quad (8)$$

where  $\mathcal{V}(t) = (A \sin \theta_t) \cos [\omega_0 t - f(t) + \varphi_t]$ . In the experiment, we calibrate the driving amplitude in the Hamiltonian [Eq. (8)] with the output power of the AWG by measuring the Rabi frequency of the NV center spin [38]. The amplitude modulation  $A \sin \theta_t$  and the phase modulation  $-f(t) + \varphi_t$  are synthesised by waveform programming in the AWG. The additional phase control function has the form of  $f(t) = A \int_0^t \cos \theta_\tau d\tau \cong A \cos \theta_0 \mathcal{J}_0(a_\theta)t - (4A \sin \theta_0/\omega) \mathcal{J}_1(a_\theta) \sin^2(\omega t/2)$ , where  $\mathcal{J}_{0,1}$  are the zeroth and first order Bessel functions of the first kind respectively [38]. Taking the limit  $\omega_0 \gg A$ , such an engineered microwave driving field allows us to realize the effective Hamiltonian in Eqs.(5, 7) with the designed parametric modulation [38]:

$$\mathcal{H}_{\text{eff}}(t) \cong \frac{A}{2} [\cos \theta_t \sigma_z + \sin \theta_t (\cos \varphi_t \sigma_x + \sin \varphi_t \sigma_y)]. \quad (9)$$

The coherent transition between the eigenstates of  $\mathcal{H}(\theta_0, \varphi_0)$  due to the periodic modulation, which is used to extract the QGT [28, 38], is detected by rotating the NV center spin around the axis  $\hat{n}(\varphi_0)$  by an angle  $2\pi - \theta_0$ . This rotation maps the eigenstates of  $\mathcal{H}(\theta_0, \varphi_0)$  back to the NV center spin state  $|0\rangle$  and  $|-1\rangle$ , which is then measured by spin-dependent fluorescence.

In the experiment, we perform a resonant parametric modulation and monitor the resulting Rabi oscillation. After preparing the NV center spin in the eigenstate  $|n(\theta_0, \varphi_0)\rangle$  of the Hamiltonian  $\mathcal{H}(\theta_0, \varphi_0)$ , we apply the engineered microwave driving field with parametric modulation [Eq. (8)] and fix the time duration  $T$ . We sweep the parametric modulation frequency  $\omega$ , and measure the probability  $p_0(T)$  that the NV center spin remains in the initial eigenstate  $|n(\theta_0, \varphi_0)\rangle$ . In Fig. 1(E), we show an example of such a parametric-modulation measurement, which corresponds to a linear modulation; see Ref. [38] for the experimental data using other types of modulations. The results indicate that a coherent transition between the eigenstates becomes resonant when  $\omega \cong A \equiv \omega_c$ . We then measure the resonant coherent oscillation upon parametric modulation with  $\omega = \omega_c$ , as shown in Fig.2 (A-C). Such dynamical responses will be shown to represent direct signatures of the system's quantum geometry.

We first consider the Rabi frequency associated with the "linear" modulation, denoted as  $\Omega_I(a_\theta, a_\varphi)$ , in view of probing the quantum metric [28]. Following a perturbative treatment [38], one obtains a relation between  $\Omega_I(a_\theta, a_\varphi)$  and the following matrix elements

$$\Omega_I(a_\theta, a_\varphi) = |\langle m | a_\theta \partial_\theta \mathcal{H}(\theta, \varphi) + a_\varphi \partial_\varphi \mathcal{H}(\theta, \varphi) | n \rangle|, \quad (10)$$

where the operators are defined in Eq. (7). Then, using Eq. (3), one can relate the matrix elements  $|\langle m | \partial_\mu \mathcal{H}(\theta, \varphi) | n \rangle|$  entering Eq. (10) to the diagonal elements of the Fubini-Study metric

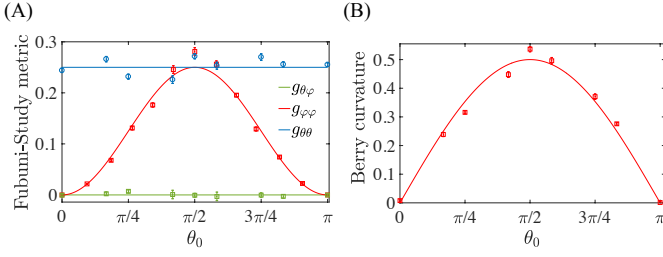


FIG. 3. **Extraction of the complete quantum geometric tensor.** (A) shows the Fubini-Study metric measured experimentally as compared with the theoretical values  $g_{\theta\varphi} = 0$  (green curve),  $g_{\varphi\varphi} = \sin^2 \theta_0/4$  (red curve) and  $g_{\theta\theta} = 1/4$  (blue curve). (B) The measured local Berry curvature  $\mathcal{F}_{\theta\varphi}$  shows good agreement with the theoretical values  $\mathcal{F}_{\theta\varphi} = \sin \theta_0/2$ . The experimental parameters are the same as Fig. 2.

$g_{\theta\theta}$  and  $g_{\varphi\varphi}$ ; see Refs. [28, 38]. In particular, when modulating a single parameter, i.e.  $a_\theta = 0$  or  $a_\varphi = 0$ , Eq. (10) reduces to  $\Omega_I(a_\theta, 0) = a_\theta \omega_c/2$  and  $\Omega_I(0, a_\varphi) = a_\varphi \omega_c \sin \theta_0/2$ . Fig. 2(D) shows the measured Rabi frequencies together with their theoretical predictions, demonstrating good agreement; this agreement can be improved by increasing the measurement time, which allows for a better determination of the oscillation frequency.

We proceed by applying a more general linear modulation with  $a_\theta, a_\varphi \neq 0$ . The induced Rabi oscillation has contributions from the individual parametric modulations, but also from their interference captured by  $\text{Re}\{\langle m|a_\theta \partial_\theta \mathcal{H}(\theta, \varphi)|n\rangle \langle n|a_\varphi \partial_\varphi \mathcal{H}(\theta, \varphi)|m\rangle\}$ ; see Eq.(10); the latter are found to be related to the off-diagonal elements [28, 38] of the Fubini-Study metric  $g_{\theta\varphi}$ . Fig. 2(E) displays the observed Rabi frequency for  $a_\varphi = \pm a_\theta$ , which demonstrate good agreement with the theoretical values  $\Omega_I(a_\theta, a_\varphi) = (a_\theta^2 + a_\varphi^2 \sin^2 \theta_0)^{1/2} \omega_c/2$ ; see Ref. [38]. Similarly, the resonant elliptical parametric modulation  $\theta_t = \theta_0 + a_\theta \sin(\omega t)$ ,  $\varphi_t = \varphi_0 + a_\varphi \cos(\omega t)$ , induces a coherent transition, with a Rabi frequency given by

$$\Omega_c(a_\theta, a_\varphi) = |\langle m|a_\theta \partial_\theta \mathcal{H}(\theta, \varphi) - i a_\varphi \partial_\varphi \mathcal{H}(\theta, \varphi)|n\rangle|. \quad (11)$$

By exploiting the interference of the two individual parametric modulations, one can extract the local Berry curvature through  $\mathcal{F}_{\theta\varphi} \sim \text{Im}\{\langle m|a_\theta \partial_\theta \mathcal{H}(\theta, \varphi)|n\rangle \langle n|a_\varphi \partial_\varphi \mathcal{H}(\theta, \varphi)|m\rangle\}$ . In Fig. 2(F), we plot the observed Rabi frequencies for  $a_\varphi = \pm a_\theta$ , which show good agreement with the theoretical values  $\Omega_c(a_\theta, a_\varphi) = |a_\theta + a_\varphi \sin \theta| \omega_c/2$  [38].

As a central result, we show in Fig. 3 the experimental extraction of the full QGT, which is based on our Rabi-oscillation measurements. This demonstrates how the coherent response upon parametric modulations provides a powerful tool to access the complete geometry of a discrete quantum system. We point out that the present method, which measures all the elements of the QGT, is based on coherent dynamical responses upon periodic parametric modulations, and in this sense, it does not rely on any adiabaticity constraints (i.e. small modulation velocity [29, 30])). Furthermore, in contrast with the

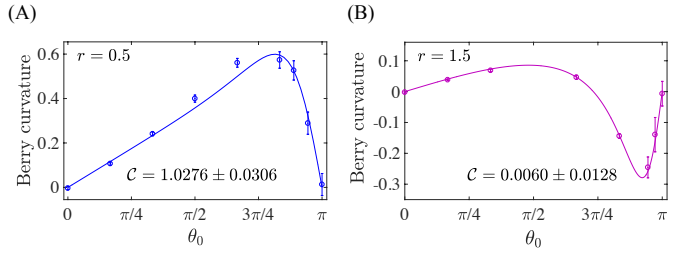


FIG. 4. **Berry curvature measurement across the topological transition.** (A-B) show the measured local Berry curvature  $\mathcal{F}_{\theta\varphi}$  for the Hamiltonian Eq.(12) describing a Dirac monopole located inside (A,  $r = 0.5$ ) and outside (B,  $r = 1.5$ ) the sphere. The curves represent the corresponding theoretical values.

excitation-rate measurement of Refs. [27, 28, 34], the QGT is extracted from Rabi oscillations [32], where the initial state is recovered after each Rabi period; in principle, this allows for the detection of geometry and topology through a non-destructive measurement.

Besides, our quantum-geometry measurement can also be used to characterize the topology of the underlying system. For this analysis, we extend the Hamiltonian to the form

$$\mathcal{H}(\theta, \varphi) = \frac{A}{2} \begin{pmatrix} \cos \theta + r & \sin \theta e^{-i\varphi} \\ \sin \theta e^{i\varphi} & -\cos \theta - r \end{pmatrix}, \quad (12)$$

where  $r$  is a tunable parameter. As for Eq. (5), the geometry of the Hamiltonian in Eq. (12) is that of a fictitious monopole located close to a sphere  $S^2$ , whose position in parametric space depends on  $r$ . The topology of the system then relies on whether this fictitious monopole is located inside the sphere or not, as captured by the Chern number  $C = \frac{1}{2\pi} \int_{S^2} \mathcal{F}_{\theta\varphi} d\theta d\varphi$ . Fig. 4 shows the Berry-curvature measurement in two distinct topological phases, and demonstrate good agreement with the theoretical predictions. In the non-trivial regime, the Chern number can equally be determined from the metric  $C = \frac{1}{2\pi} \int_{S^2} (2\sqrt{\bar{g}}) d\theta d\varphi = \frac{1}{2\pi} \int_{S^2} |\mathcal{F}_{\theta\varphi}| d\theta d\varphi$ , where  $\bar{g} = g_{\theta\theta}g_{\varphi\varphi} - g_{\theta\varphi}^2$  is the determinant of the QGT [19]. Altogether, these results indicate that topology can indeed be finely analyzed based on our geometric-detection scheme.

*Conclusion & outlook.*— To summarize, we have experimentally demonstrated a powerful connection between coherent excitations upon parametric modulations and the quantum geometric tensor. Based on such a fundamental relation, we have extracted the complete quantum geometric tensor of a quantum system, which includes all the components of the Fubini-Study metric and those of the local Berry curvature. The method is readily applicable to observe other intriguing topological defects, such as tensor monopoles defined in 4D parameter spaces [19], and could also be further extended to two coupled qubits. The results demonstrate that coherent dynamical response can serve as a powerful tool to access the geometric and topological properties of quantum systems, and opens a way to explore the fundamental role of the quantum geometric tensor in various scenarios, ranging from many-body

systems to open quantum systems.

*Acknowledgments.*— We thank G. Palumbo, M. Di Liberto, P. Zoller for helpful discussions. The work is supported by National Natural Science Foundation of China (11574103, 11690030, 11690032, 11874024), National 1000 Youth Talent Program. M.B.P. is supported by the EU projects HYPERDIAMOND and AsteriQs, the BMBF project NanoSpin and DiaPol and the ERC Synergy grant BioQ. F. J. is supported by DFG (FOR 1493, SPP 1923), VW Stiftung, BMBF, ERC, EU (AsteriQs), BW Stiftung, Ministry of Science and Arts, Center for Integrated quantum science and technology (IQST). T.O. is supported by JSPS KAKENHI Grant Number JP18H05857, RIKEN Incentive Research Project, and the Interdisciplinary Theoretical and Mathematical Sciences Program (iTHEMS) at RIKEN. N.G. is supported by the ERC Starting Grant TopoCold and the Fonds De La Recherche Scientifique (FRS-FNRS)(Belgium).

\* These authors contributed equally

† [shaoliang@hust.edu.cn](mailto:shaoliang@hust.edu.cn)

‡ [jianmingcai@hust.edu.cn](mailto:jianmingcai@hust.edu.cn)

- [1] T. W. B. Kibble, Geometrization of quantum mechanics. *Comm. Math. Phys.* **65**, 189 (1979).
- [2] J. Provost and G. Vallee, Riemannian structure on manifolds of quantum states. *Commun. Math. Phys.* **76**, 289 (1980).
- [3] J. Anandan and Y. Aharonov, Geometry of quantum evolution. *Phys. Rev. Lett.* **65**, 1697 (1990).
- [4] D. C. Brody, L. P. Hughston, Geometric quantum mechanics. *J. Geom. Phys.* **38**, 19-53 (2001).
- [5] M. Kolodrubetz, D. Sels, P. Mehta, and A. Polkovnikov, Geometry and non-adiabatic response in quantum and classical system. *Phys. Rep.* **697**, 1 (2017).
- [6] B. Simon, Holonomy, the quantum adiabatic theorem, and Berry's phase. *Phys. Rev. Lett.* **51**, 2167 (1984).
- [7] M. Berry, Quantal phase factors accompanying adiabatic changes. *Proc. R. Soc. London, Ser. A* **392**, 45 (1984).
- [8] A. Bohm, A. Mostafazadeh, H. Koizumi, Q. Niu, J. Zwanziger, *The Geometric Phase in Quantum Systems: Foundations, Mathematical Concepts, and Applications in Molecular and Condensed Matter Physics* (Springer Science & Business Media 2013).
- [9] N. Nagaosa, J. Sinova, S. Onoda, A. H. MacDonald, N. P. Ong, Anomalous Hall effect. *Rev. Mod. Phys.* **82**, 1539, (2010).
- [10] M. Z. Hasan and C. L. Kane, Topological insulators. *Rev. Mod. Phys.* **82**, 3045 (2010).
- [11] P. Zanardi, P. Giorda, and M. Cozzini, Information-theoretic differential geometry of quantum phase transitions. *Phys. Rev. Lett.* **99**, 100603 (2007).
- [12] V. V. Albert, B. Bradlyn, M. Fraas, and L. Jiang, Geometry and response of Lindbladians. *Phys. Rev. X* **6**, 041031 (2016).
- [13] Y. Gao, S. A. Yang, and Q. Niu, Geometrical effects in orbital magnetic susceptibility. *Phys. Rev. B* **91**, 214405 (2015).
- [14] F. Piéchon, A. Raoux, J.-N. Fuchs, and G. Montambaux, Geometric orbital susceptibility: Quantum metric without Berry curvature. *Phys. Rev. B* **94**, 134423 (2016).
- [15] I. Souza, T. Wilkens, and R. M. Martin, Polarization and localization in insulators: Generating function approach. *Phys. Rev. B* **62**, 1666 (2000).
- [16] A. Srivastava and A. Imamoğlu, Signatures of Bloch-band geometry on excitons: Nonhydrogenic spectra in transition-metal Dichalcogenides. *Phys. Rev. Lett.* **115**, 166802 (2015).
- [17] A. Julku, S. Peotta, T. I. Vanhala, D.-H. Kim, and P. Törmä, Geometric origin of superfluidity in the Lieb-Lattice flat band. *Phys. Rev. Lett.* **117**, 045303 (2016).
- [18] R. Roy, Band geometry of fractional topological insulators. *Phys. Rev. B* **90**, 165139 (2014).
- [19] G. Palumbo, N. Goldman, Revealing tensor monopoles through quantum-metric measurements. *Phys. Rev. Lett.* **121**, 170401 (2018).
- [20] T. Li, L. Duca, M. Reitter, F. Grusdt, E. Demler, M. Endres, M. Schleier-Smith, I. Bloch, U. Schneider, Bloch state tomography using Wilson lines. *Science* **352**, 1094 (2016).
- [21] L. Duca, T. Li, M. Reitter, I. Bloch, M. Schleier-Smith, U. Schneider, An Aharonov-Bohm interferometer for determining Bloch band topology. *Science* **347**, 288 (2015).
- [22] N. Fläschner, B. S. Rem, M. Tarnowski, D. Vogel, D.-S. Lühmann, K. Sengstock, C. Weitenberg, Experimental reconstruction of the Berry curvature in a Floquet Bloch band. *Science* **352**, 1091 (2016).
- [23] M. Wimmer, H. M. Price, I. Carusotto, and U. Peschel, Experimental measurement of the Berry curvature from anomalous transport. *Nature Physics*, **13**, 545 (2017).
- [24] H. B. Banks, Q. Wu, D. C. Valocin, S. Mack, A. C. Gosard, L. Pfeiffer, R.-B. Liu, and M. S. Sherwin, Dynamical Birefringence: Electron-hole recollisions as probes of Berry curvature. *Phys. Rev. X*, **7**, 041042 (2017).
- [25] T. T. Luu, and H. J. Wörner, Measurement of the Berry curvature of solids using high-harmonic spectroscopy. *Nat. Commun.*, **9**, 916 (2018).
- [26] N. Marzari and D. Vanderbilt, Maximally localized generalized Wannier functions for composite energy bands. *Phys. Rev. B* **56**, 12847 (1997).
- [27] L. Asteria, D. T. Tran, T. Ozawa, M. Tarnowski, B. S. Rem, N. Fläschner, K. Sengstock, N. Goldman, C. Weitenberg, Measuring quantized circular dichroism in ultracold topological matter. arXiv:1805.11077.
- [28] T. Ozawa and N. Goldman, Extracting the quantum metric tensor through periodic driving. *Phys. Rev. B* **97**, 201117(R) (2018).
- [29] P. Roushan, C. Neill, Y. Chen, M. Kolodrubetz, C. Quintana, N. Leung, M. Fang, R. Barends, B. Campbell, Z. Chen, B. Chiaro, A. Dunsworth, E. Jeffrey, J. Kelly, A. Megrant, J. Mutus, P. J. J. O'Malley, D. Sank, A. Vainsencher, J. Wenner, T. White, A. Polkovnikov, A. N. Cleland, and J. M. Martinis, Observation of topological transitions in interacting quantum circuits. *Nature* **515**, 241 (2014).
- [30] V. Gritsev and A. Polkovnikov, Dynamical quantum Hall effect in the parameter space. *Proc. Natl. Acad. Sci. USA* **109**, 6457 (2012).
- [31] M. D. Schroer, M. H. Kolodrubetz, W. F. Kindel, M. Sandberg, J. Gao, M. R. Vissers, D. P. Pappas, A. Polkovnikov, and K. W. Lehnert, Measuring a topological transition in an artificial spin-1/2 system. *Phys. Rev. Lett.* **113**, 050402 (2014).
- [32] D. T. Tran, N. R. Cooper, N. Goldman, Quantized Rabi oscillations and circular dichroism in quantum Hall systems. *Phys. Rev. A* **97**, 061602 (2018).
- [33] F. de Juan, A. G. Grushin, T. Morimoto, and J. E. Moore, Quantized circular photogalvanic effect in Weyl semimetals. *Nat. Commun.* **8**, 15995 (2017).
- [34] D. T. Tran, A. Dauphin, A. G. Grushin, P. Zoller, and N. Goldman, Probing topology by "heating": Quantized circular dichroism in ultracold atoms. *Sci. Adv.* **3**, e1701207 (2017).
- [35] C. Wang, P. Zhang, X. Chen, J. Yu, and H. Zhai, Scheme to mea-

- sure the topological number of a Chern insulator from quench dynamics. *Phys. Rev. Lett.* **118**, 185701 (2017).
- [36] N. Fläschner, D. Vogel, M. Tarnowski, B. S. Rem, D.-S. Lühmann, M. Heyl, J. C. Budich, L. Mathey, K. Sengstock, and C. Weitenberg, Observation of dynamical vortices after quenches in a system with topology. *Nat. Phys.* **14**, 265 (2018).
- [37] M. Tarnowski, F. N. Únal, N. Fläschner, B. S. Rem, A. Eckardt, K. Sengstock, and C. Weitenberg, Characterizing topology by dynamics: Chern number from linking number. arXiv: 1709.01046.
- [38] Further details on the experiments and additional data are available as supplementary material.

## APPENDIX

### A. Parametric modulation induced coherent transition for discrete quantum systems

In the main text, we experimentally demonstrate the connection between parametric modulation induced coherent transition and quantum geometric tensor for discrete quantum systems. Here, we provide a detailed analysis on such a fundamental connection following Ref. (28). Consider a discrete quantum system with a general Hamiltonian  $\mathcal{H}(\boldsymbol{\lambda})$  which depends on a set of dimensionless parameters  $\boldsymbol{\lambda} = (\lambda_1, \lambda_2, \dots, \lambda_N)$  where  $N$  is the dimension of parameter space, the eigenstates are given as follows

$$\mathcal{H}(\boldsymbol{\lambda})|n(\boldsymbol{\lambda})\rangle = \epsilon_n(\boldsymbol{\lambda})|n(\boldsymbol{\lambda})\rangle \quad (\text{S.1})$$

If the Hamiltonian has no energy degeneracy, the definition of quantum geometric tensor (QGT) is (5)

$$\chi_{\mu\nu} = \langle \partial_\mu n(\boldsymbol{\lambda}) | (1 - |n(\boldsymbol{\lambda})\rangle\langle n(\boldsymbol{\lambda})|) | \partial_\nu n(\boldsymbol{\lambda}) \rangle. \quad (\text{S.2})$$

For simplicity, we denote  $\partial_\mu \equiv \partial_{\lambda_\mu}$  hereafter in the main text and supplementary information. The real part of QGT  $\text{Re}(\chi_{\mu\nu}) = g_{\mu\nu}$  is the Fubini-Study metric that quantifies the distance between nearby states  $|n(\boldsymbol{\lambda})\rangle$  and  $|n(\boldsymbol{\lambda} + d\boldsymbol{\lambda})\rangle$  on parametric manifold, the imaginary part  $\text{Im}(\chi_{\mu\nu}) = -\mathcal{F}_{\mu\nu}(\boldsymbol{\lambda})/2$  where  $\mathcal{F}_{\mu\nu}(\boldsymbol{\lambda})$  is the local Berry curvature, which is responsible for the geometric (Berry) phase. The QGT is shown to connect with the coherent response on parametric modulation (28). In the main text, we consider two types of parametric modulation  $[\lambda_\mu(t), \lambda_\nu(t)]$ : (a) the linear parametric modulation with  $\lambda_\mu(t) = \lambda_\mu^0 + a_\mu \sin(\omega t)$ ,  $\lambda_\nu(t) = \lambda_\nu^0 + a_\nu \sin(\omega t)$ ; (b) the elliptical parametric modulation with  $\lambda_\mu(t) = \lambda_\mu^0 + a_\mu \sin(\omega t)$ ,  $\lambda_\nu(t) = \lambda_\nu^0 + a_\nu \cos(\omega t)$ .

As a specific example of linear parametric modulation with  $a_\mu \neq 0$  and  $a_\nu = 0$ , when considering weak parametric modulation i.e.  $a_\mu \ll 1$ , the time-dependent Hamiltonian can be expanded as

$$\mathcal{H}[\boldsymbol{\lambda}(t)] = \mathcal{H}(\boldsymbol{\lambda}^0) + a_\mu [\partial_\mu \mathcal{H}(\boldsymbol{\lambda}^0)] \sin(\omega t) \quad (\text{S.3})$$

Assume that the initial state is prepared on the ground state  $|n(\boldsymbol{\lambda}^0)\rangle$ , it will be excited onto the higher energy levels by the time-dependent Hamiltonian. Since the Hamiltonian is periodic, the problem can be solved by Floquet theorem. But if the frequency of modulation is on resonance with the energy detuning between  $|n(\boldsymbol{\lambda}^0)\rangle$  and  $|m(\boldsymbol{\lambda}^0)\rangle$  namely  $\hbar\omega = \hbar\omega_{n \leftrightarrow m} \equiv |\epsilon_m(\boldsymbol{\lambda}^0) - \epsilon_n(\boldsymbol{\lambda}^0)|$ , the Floquet Hamiltonian can be simplified as a two-level Hamiltonian in the Hilbert subspace spanned by  $\{|n(\boldsymbol{\lambda}^0)\rangle, |m(\boldsymbol{\lambda}^0)\rangle\}$  as follows

$$\mathcal{H}_{\text{rot}}(\boldsymbol{\lambda}^0) = \begin{pmatrix} \epsilon_m(\boldsymbol{\lambda}^0) - \hbar\omega & \Omega_{n \leftrightarrow m}(\boldsymbol{\lambda}^0) \\ \Omega_{n \leftrightarrow m}^*(\boldsymbol{\lambda}^0) & \epsilon_n(\boldsymbol{\lambda}^0) \end{pmatrix}, \quad (\text{S.4})$$

where

$$\Omega_{n \leftrightarrow m}(\boldsymbol{\lambda}^0) = \frac{a_\mu}{2} \langle m(\boldsymbol{\lambda}^0) | \partial_\mu \mathcal{H}(\boldsymbol{\lambda}^0) | n(\boldsymbol{\lambda}^0) \rangle, \quad (\text{S.5})$$

with the following relation as

$$|\langle m(\boldsymbol{\lambda}^0) | \partial_\mu \mathcal{H}(\boldsymbol{\lambda}^0) | n(\boldsymbol{\lambda}^0) \rangle|^2 = [\epsilon_m(\boldsymbol{\lambda}^0) - \epsilon_n(\boldsymbol{\lambda}^0)]^2 \langle \partial_\mu n(\boldsymbol{\lambda}^0) | m(\boldsymbol{\lambda}^0) \rangle \langle m(\boldsymbol{\lambda}^0) | \partial_\mu n(\boldsymbol{\lambda}^0) \rangle. \quad (\text{S.6})$$

According to the definition of QGT, it can be seen that the diagonal element of the Fubini-Study metric can be expressed as follows

$$g_{\mu\mu}(\boldsymbol{\lambda}) = \langle \partial_\mu n(\boldsymbol{\lambda}) | (1 - |n(\boldsymbol{\lambda})\rangle\langle n(\boldsymbol{\lambda})|) | \partial_\mu n(\boldsymbol{\lambda}) \rangle \quad (\text{S.7})$$

$$= \sum_{m \neq n} \langle \partial_\mu n(\boldsymbol{\lambda}) | m(\boldsymbol{\lambda}) \rangle \langle m(\boldsymbol{\lambda}) | \partial_\mu n(\boldsymbol{\lambda}) \rangle \quad (\text{S.8})$$

$$= \sum_{m \neq n} \frac{|\langle m(\boldsymbol{\lambda}) | \partial_\mu \mathcal{H}(\boldsymbol{\lambda}) | n(\boldsymbol{\lambda}) \rangle|^2}{(\epsilon_m(\boldsymbol{\lambda}) - \epsilon_n(\boldsymbol{\lambda}))^2} \quad (\text{S.9})$$

$$= \sum_{m \neq n} \frac{4|\Omega_{n \leftrightarrow m}(\boldsymbol{\lambda})|^2}{a_\mu^2 \omega_{n \leftrightarrow m}^2}. \quad (\text{S.10})$$

For a two-level quantum system, the Rabi frequency of coherence transition is

$$\Omega_I(a_\mu) = 2|\Omega_{n \leftrightarrow m}(\boldsymbol{\lambda})| = a_\mu g_{\mu\mu}^{1/2}(\boldsymbol{\lambda}) \omega_c, \quad (\text{S.11})$$

where  $\omega_c = \omega_{g \leftrightarrow e}$  represents the resonant frequency between the ground state and the excited state.

We proceed to consider general linear parametric modulation  $\boldsymbol{\lambda}_\mu(t) = \boldsymbol{\lambda}_\mu^0 + a_\mu \sin(\omega t)$ ,  $\boldsymbol{\lambda}_\nu(t) = \boldsymbol{\lambda}_\nu^0 + a_\nu \sin(\omega t)$  with  $a_\mu \neq 0$  and  $a_\nu \neq 0$ . The amplitude of parametric modulation is small  $|a_\mu|, |a_\nu| \ll 1$ , thus the time-dependent Hamiltonian can be written as follows

$$\mathcal{H}[\boldsymbol{\lambda}(t)] = \mathcal{H}(\boldsymbol{\lambda}^0) + a_\mu [\partial_\mu \mathcal{H}(\boldsymbol{\lambda}^0)] \sin(\omega t) + a_\nu [\partial_\nu \mathcal{H}(\boldsymbol{\lambda}^0)] \sin(\omega t). \quad (\text{S.12})$$

And the coherent transition Rabi frequency is

$$\Omega_{n \leftrightarrow m}(\boldsymbol{\lambda}) = \frac{1}{2} \langle m(\boldsymbol{\lambda}) | a_\mu \partial_\mu \mathcal{H}(\boldsymbol{\lambda}) + a_\nu \partial_\nu \mathcal{H}(\boldsymbol{\lambda}) | n(\boldsymbol{\lambda}) \rangle. \quad (\text{S.13})$$

Similarly, we can get the following relation between parametric modulation induced coherent transition and the Fubini-Study metric as

$$\sum_{m \neq n} \frac{4|\Omega_{n \leftrightarrow m}(\boldsymbol{\lambda})|^2}{\omega_{n \leftrightarrow m}^2} = a_\mu^2 g_{\mu\mu} + 2a_\mu a_\nu g_{\mu\nu} + a_\nu^2 g_{\nu\nu}. \quad (\text{S.14})$$

In particular, for a two-level quantum system, the corresponding Rabi frequency of coherent transition  $\Omega_I(a_\mu, a_\nu) = 2|\Omega_{n \leftrightarrow m}(\boldsymbol{\lambda})|$  is related to the Fubini-Study metric as follows

$$\Omega_I(a_\mu, a_\nu)^2 / \omega_{g \leftrightarrow e}^2 = a_\mu^2 g_{\mu\mu} + 2a_\mu a_\nu g_{\mu\nu} + a_\nu^2 g_{\nu\nu}. \quad (\text{S.15})$$

Therefore, one can extract the off-diagonal element of the Fubini-Study metric as follows

$$g_{\mu\nu} = [\Omega_I(a_\mu, a_\nu)^2 - \Omega_I(a_\mu, -a_\nu)^2] / (4a_\mu a_\nu \omega_{g \leftrightarrow e}^2). \quad (\text{S.16})$$

The coherent response on the elliptical parametric modulation with  $\boldsymbol{\lambda}_\mu(t) = \boldsymbol{\lambda}_\mu^0 + a_\mu \sin(\omega t)$ ,  $\boldsymbol{\lambda}_\nu(t) = \boldsymbol{\lambda}_\nu^0 + a_\nu \cos(\omega t)$  can be analysed in a similar way. The corresponding time-dependent Hamiltonian can be written as follows

$$\mathcal{H}[\boldsymbol{\lambda}(t)] = \mathcal{H}(\boldsymbol{\lambda}^0) + a_\mu [\partial_\mu \mathcal{H}(\boldsymbol{\lambda}^0)] \sin(\omega t) + a_\nu [\partial_\nu \mathcal{H}(\boldsymbol{\lambda}^0)] \cos(\omega t). \quad (\text{S.17})$$

The coherent transition Rabi frequency is

$$\Omega_{n \leftrightarrow m}(\boldsymbol{\lambda}) = \frac{1}{2} \langle m(\boldsymbol{\lambda}) | a_\mu \partial_\mu \mathcal{H}(\boldsymbol{\lambda}) - i a_\nu \partial_\nu \mathcal{H}(\boldsymbol{\lambda}) | n(\boldsymbol{\lambda}) \rangle, \quad (\text{S.18})$$

which is connected with the local Berry curvature as

$$\sum_{m \neq n} \frac{4|\Omega_{n \leftrightarrow m}(\boldsymbol{\lambda})|^2}{\omega_{n \leftrightarrow m}^2} = a_\mu^2 g_{\mu\mu} + a_\mu a_\nu \mathcal{F}_{\mu\nu} + a_\nu^2 g_{\nu\nu}. \quad (\text{S.19})$$

For a two-level quantum system, we have the Rabi frequency of coherent transition  $\Omega_c(a_\mu, a_\nu) = 2|\Omega_{n \leftrightarrow m}(\boldsymbol{\lambda})|$  is related to the Fubini-Study metric and the local Berry curvature as follows

$$\Omega_c(a_\mu, a_\nu)^2 / \omega_{g \leftrightarrow e}^2 = a_\mu^2 g_{\mu\mu} + a_\mu a_\nu \mathcal{F}_{\mu\nu} + a_\nu^2 g_{\nu\nu}. \quad (\text{S.20})$$

Therefore, one can measure the local Berry curvature in the following way

$$\mathcal{F}_{\mu\nu} = [\Omega_c(a_\mu, a_\nu)^2 - \Omega_c(a_\mu, -a_\nu)^2] / (2a_\mu a_\nu \omega_{g \leftrightarrow e}^2). \quad (\text{S.21})$$

We remark that, for a discrete quantum system with more than two energy levels, the frequency shall be modulated in a larger range and a series of resonant transitions from the specific eigenstate to the other eigenstates shall be taken into account respectively. In the limit  $a_\mu, a_\nu \ll 1$  where  $\mu, \nu \in \{\lambda_1, \lambda_2, \dots, \lambda_N\}$ , each resonant transition can be approximated as a two-level system and the transition element  $\langle m(\lambda) | \partial_\mu \mathcal{H}(\lambda) | n(\lambda) \rangle$  (see Eq.3 in the main text) can be measured similarly.

### B. Floquet analysis of coherent response on parametric modulation

The Hamiltonian of a two-level quantum system that we realize in the main text is in the parameter space and can be written as

$$\mathcal{H}(\theta, \varphi) = \frac{A}{2} \begin{pmatrix} \cos \theta & \sin \theta e^{-i\varphi} \\ \sin \theta e^{i\varphi} & -\cos \theta \end{pmatrix}. \quad (\text{S.22})$$

The system's response to periodic parametric modulation reveals information on quantum geometry. Here, we provide Floquet analysis for the example of linear parametric modulation  $\theta(t) = \theta_0 + a_\theta \sin(\omega t)$ ,  $\varphi(t) = \varphi_0 + a_\varphi \sin(\omega t)$  with  $a_\theta = 0$  and  $a_\varphi \neq 0$ . In this case, the time-dependent Hamiltonian can be expanded as

$$\mathcal{H}(t) = \mathcal{H}_0(\theta_0, \varphi_0) + \sum_{n \neq 0} \mathcal{H}_n e^{in\omega t} \quad (\text{S.23})$$

with

$$\mathcal{H}_n = \frac{A}{2} \mathcal{J}_n(a_\varphi) \sin \theta_0 \begin{pmatrix} 0 & e^{-i\varphi_0} \\ (-1)^n e^{i\varphi_0} & 0 \end{pmatrix}, \quad (\text{S.24})$$

where  $\mathcal{J}_n$  is the n-th order Bessel function of the first kind. The eigenstates of the Hamiltonian  $\mathcal{H}_0(\theta_0, \varphi_0)$  are

$$|\psi_1\rangle = \cos \frac{\theta_0}{2} |\uparrow\rangle + \sin \frac{\theta_0}{2} e^{i\varphi_0} |\downarrow\rangle, \quad (\text{S.25})$$

$$|\psi_2\rangle = -\sin \frac{\theta_0}{2} e^{-i\varphi_0} |\uparrow\rangle + \cos \frac{\theta_0}{2} |\downarrow\rangle, \quad (\text{S.26})$$

with the corresponding eigenenergy  $\pm \frac{A}{2}$  respectively. Then one can rotate the above time-dependent Hamiltonian written in the basis  $\{|\psi_1\rangle, |\psi_2\rangle\}$  as

$$\mathcal{H}'(t) = \frac{A}{2} (|\psi_1\rangle\langle\psi_1| - |\psi_2\rangle\langle\psi_2|) + \sum_{n \neq 0} \mathcal{H}'_n e^{in\omega t}, \quad (\text{S.27})$$

where

$$\mathcal{H}'_{2n-1} = \frac{A}{2} \mathcal{J}_{2n-1}(a_\varphi) \sin \theta_0 \begin{pmatrix} 0 & e^{-i\varphi_0} \\ -e^{i\varphi_0} & 0 \end{pmatrix}, \quad \mathcal{H}'_{2n} = \frac{A}{2} \mathcal{J}_{2n}(a_\varphi) \sin \theta_0 \begin{pmatrix} \sin \theta_0 & \cos \theta_0 e^{-i\varphi_0} \\ \cos \theta_0 e^{i\varphi_0} & -\sin \theta_0 \end{pmatrix}. \quad (\text{S.28})$$

Under rotating wave approximation, in the resonance case  $\hbar\omega \cong A$ , the higher order terms can be ignored and the above Hamiltonian can be simplified as

$$\mathcal{H}'(t) = \frac{A}{2} (|\psi_1\rangle\langle\psi_1| - |\psi_2\rangle\langle\psi_2|) + \frac{A}{2} \mathcal{J}_1(a_\varphi) \sin \theta_0 e^{i\omega t} (e^{-i\varphi_0} |\psi_1\rangle\langle\psi_2| - e^{i\varphi_0} |\psi_2\rangle\langle\psi_1|) + h.c. \quad (\text{S.29})$$

which leads to the following effective Hamiltonian as

$$\mathcal{H}_{\text{rot}} = \begin{pmatrix} \frac{A}{2} & -\frac{A}{2} \mathcal{J}_1(a_\varphi) \sin \theta_0 e^{i\varphi_0} \\ -\frac{A}{2} \mathcal{J}_1(a_\varphi) \sin \theta_0 e^{-i\varphi_0} & -\frac{A}{2} + \hbar\omega \end{pmatrix}. \quad (\text{S.30})$$

Therefore, the Rabi frequency of coherent transition from the ground state to the excited state is

$$\Omega = \frac{A}{2} \mathcal{J}_1(a_\varphi) \sin \theta_0 = a_\varphi g_{\varphi\varphi}^{1/2} \omega_c / 2. \quad (\text{S.31})$$

We remark that the above Floquet analysis can be extended to general linear parametric modulation as well as elliptical parametric modulation.

### C. Engineering of the effective Hamiltonian with parametric modulation

In the main text, we engineer a microwave driving field with amplitude, frequency and phase modulation (see Eq.5) acting on the NV center spin that leads to the following Hamiltonian as

$$\mathcal{H}(t) = \frac{\omega_0}{2}\sigma_z + A \sin \theta_t \cos [\omega_0 t - f(t) + \varphi_t] \sigma_x, \quad (\text{S.32})$$

where  $\theta_t$  and  $\varphi_t$  are periodically modulated parameters and  $f(t)$  is a function which can be controlled in experiment. We first define the operator

$$\mathcal{K}(t) = \frac{\omega_0 t}{2}\sigma_z - \frac{A}{2} \int_0^t \cos \theta_\tau d\tau \sigma_z \equiv \mathcal{A}(t)\sigma_z \quad (\text{S.33})$$

The effective Hamiltonian in the rotating frame can be written as

$$\mathcal{H}_{\text{eff}} = e^{i\mathcal{K}(t)}\mathcal{H}(t)e^{-i\mathcal{K}(t)} + i\left(\frac{\partial e^{i\mathcal{K}(t)}}{\partial t}\right)e^{-i\mathcal{K}(t)} \quad (\text{S.34})$$

$$= e^{i\mathcal{A}(t)\sigma_z} \left\{ \frac{\omega_0}{2}\sigma_z + A \sin \theta_t \cos[\omega_0 t - f(t) + \varphi_t] \sigma_x \right\} e^{-i\mathcal{A}(t)\sigma_z} - \frac{\partial \mathcal{A}(t)}{\partial t} \sigma_z \quad (\text{S.35})$$

$$= A \sin \theta_t \cos[\omega_0 t - f(t) + \varphi_t] \left\{ e^{i\mathcal{A}(t)\sigma_z} \sigma_x e^{-i\mathcal{A}(t)\sigma_z} \right\} + \frac{A}{2} \cos \theta_t \sigma_z \quad (\text{S.36})$$

$$= A \sin \theta_t \cos[\omega_0 t - f(t) + \varphi_t] \{ \cos[2\mathcal{A}(t)]\sigma_x - \sin[2\mathcal{A}(t)]\sigma_y \} + \frac{A}{2} \cos \theta_t \sigma_z \quad (\text{S.37})$$

$$\cong \frac{A}{2} \sin \theta_t \cos \left[ A \int_0^t \cos \theta_\tau d\tau - f(t) + \varphi_t \right] \sigma_x + A \sin \theta_t \sin \left[ A \int_0^t \cos \theta_\tau d\tau - f(t) + \varphi_t \right] \sigma_y + \frac{A}{2} \cos \theta_t \sigma_z, \quad (\text{S.38})$$

where we use rotating-wave approximation and neglect the fast oscillating terms with frequency  $2\omega_0$ . If we set the phase control function

$$f(t) = A \int_0^t \cos \theta_\tau d\tau, \quad (\text{S.39})$$

the effective Hamiltonian can be simplified as

$$\mathcal{H}_{\text{eff}} \cong \frac{A}{2} \left[ \cos \theta_t \sigma_z + \sin \theta_t (\cos \varphi_t \sigma_x + \sin \varphi_t \sigma_y) \right] \quad (\text{S.40})$$

which is the desired Hamiltonian. In our experiments, we implement the phase control function  $f(t)$  for  $\theta_t = \theta_0 + a_\theta \sin(\omega t)$  as follows

$$\begin{aligned} f(t) &= A \int_0^t \cos \theta_\tau d\tau \\ &= A \int_0^t \cos [\theta_0 + a_\theta \sin(\omega\tau)] d\tau \\ &= A \int_0^t \left\{ \cos \theta_0 \left[ \mathcal{J}_0(a_\theta) + 2 \sum_{n=1}^{\infty} \mathcal{J}_{2n}(a_\theta) \cos(2n\omega\tau) \right] - 2 \sin \theta_0 \sum_{n=0}^{\infty} \mathcal{J}_{2n+1}(a_\theta) \sin((2n+1)\omega\tau) \right\} \\ &\cong A \cos \theta_0 \mathcal{J}_0(a_\theta) t - \frac{4A \sin \theta_0}{\omega} \mathcal{J}_1(a_\theta) \sin^2(\omega t/2), \end{aligned} \quad (\text{S.41})$$

where  $\mathcal{J}_n(x)$  is the  $n$ -th order Bessel function of the first kind. The approximation in the last line is valid for the present scenarios with  $a_\theta \ll 1$ .

#### D. Initial state preparation and verification

In our experiments, the first step is to prepare the NV center spin into the ground state of the unperturbed Hamiltonian  $\mathcal{H}(\theta_0, \varphi_0)$  as follows

$$\mathcal{H}(\theta_0, \varphi_0) = \frac{A}{2} \begin{pmatrix} \cos \theta_0 & \sin \theta_0 e^{-i\varphi_0} \\ \sin \theta_0 e^{i\varphi_0} & -\cos \theta_0 \end{pmatrix}. \quad (\text{S.42})$$

which is a superposition state  $|\psi(0)\rangle = \cos \frac{\theta}{2} |-1\rangle + e^{i\varphi_0} \sin \frac{\theta}{2} |0\rangle$ , see Eq.(S.27), in which we denote  $|\uparrow\rangle \equiv |-1\rangle$  and  $|\downarrow\rangle \equiv |0\rangle$ . Such an initial state can be prepared by applying a resonant microwave driving field as

$$H_p = \frac{\omega_0}{2} \sigma_z + \Omega \sin(\omega_0 t + \varphi) \sigma_x, \quad (\text{S.43})$$

for time duration  $t = \theta_0/\Omega$ , where  $\Omega$  is the Rabi frequency. If the initial state is not in the eigenstate of the Hamiltonian  $\mathcal{H}(\theta_0, \varphi_0)$ , it would cause oscillation that may blur the coherent oscillation arising from parametric modulation. In order to verify that we have indeed prepared the NV center spin into the right initial state, we perform experiments by engineering a microwave driving field corresponding to the Hamiltonian in Eq.(S.42). If the initial state is the ground state of  $\mathcal{H}(\theta_0, \varphi_0)$ , no transition to the excited state will be observed. In the experiments, we carefully tune the microwave pulse duration for the initial state preparation so that no transition to the excited state under the Hamiltonian  $\mathcal{H}(\theta_0, \varphi_0)$  occurs, as shown in Fig.S1.

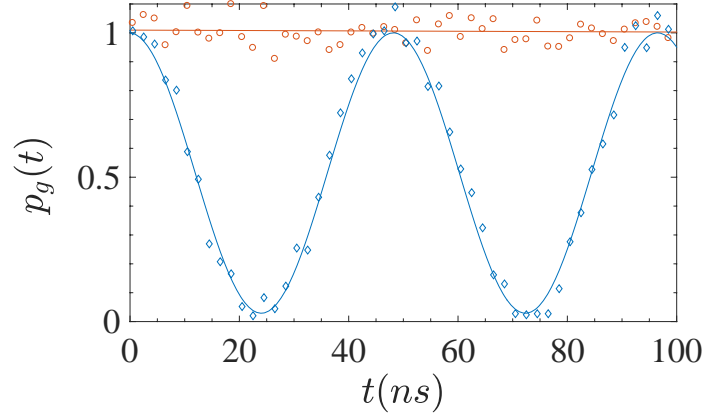


FIG. S1. **Verification of initial state preparation.** The state evolution from the initial state  $|\psi(0)\rangle$ , as governed by the Hamiltonian  $\mathcal{H}(\theta_0, \varphi_0)$ , is quantified by the fidelity  $p_g(t) = |\langle \psi(t) | \psi(0) \rangle|^2$ . The plot shows two initial states that are prepared by the microwave pulse  $\mathcal{H}_i(t) = \Omega \sin(\omega_0 t + \varphi_0) \sigma_x$  with different time duration  $t = 11.94$  ns (red,  $\circ$ ) and  $t = 0.04$  ns (blue,  $\diamond$ ).

#### E. Calibration of Rabi frequency and microwave amplitude

As we program parametric modulation in the waveform of AWG by specifying the microwave output amplitude, it is necessary to calibrate the relation between the microwave amplitude of AWG output and the Rabi frequency of the NV center spin. In Fig.S2, we show one example of such a calibration, which shows that the Rabi frequency of the NV center spin scales linear with the AWG output amplitude for the parameter regime in which our experiments are performed. The microwave calibration is done for all the measurements.

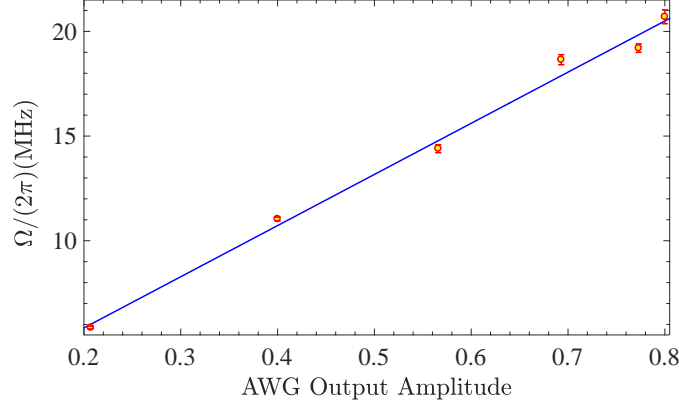


FIG. S2. **Calibration of Rabi frequency and microwave amplitude.** The measured Rabi frequency  $\Omega$  of the NV center spin as a function of the output amplitude of arbitrary waveform generator while using the same microwave amplifying efficiency.

### F. Parametric modulation resonance measurement

In the parametric modulation resonance measurement experiments, we first prepare the NV center spin in the ground state  $|\psi_0\rangle$  of the Hamiltonian  $\mathcal{H}(\theta_0, \varphi_0)$  by a microwave pulse  $\hat{n}(\varphi_0)|_{\theta_0}$ . We then apply the engineered microwave driving field with different types of parametric modulation and fix the time duration  $T$ . By sweeping the parametric modulation frequency  $\omega$ , we measure the probability  $p_0(T)$  that the NV center spin remains in the ground state  $|\psi_0\rangle$ . When the parametric modulation frequency  $\omega$  matches the transition frequency, we observe a resonance signal in the probability  $p_0(T)$ . In the main text, as shown in Fig.1(E), we provide an example of parametric modulation resonance measurement. In Fig.S3, we show the parametric modulation resonance measurement data for the other types of parametric modulation.

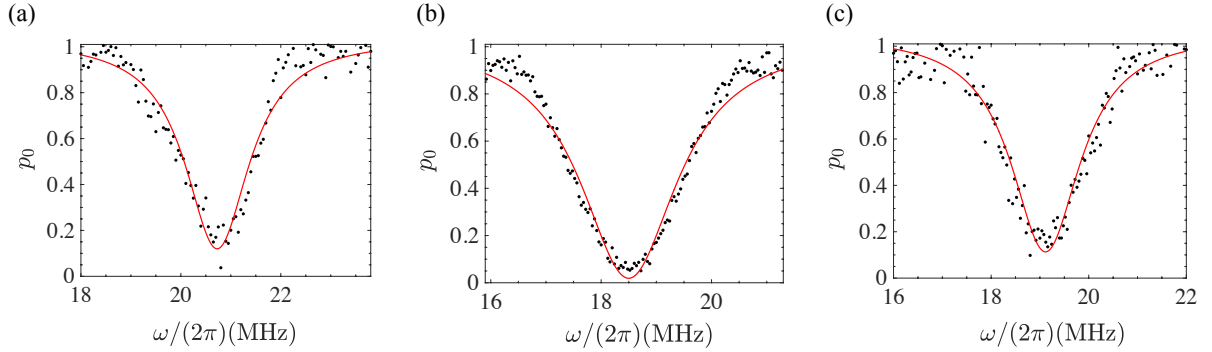


FIG. S3. **Parametric modulation resonance measurement.** The probability that the NV center spin remains in the ground state  $|\psi(g)\rangle$  at time  $T$  as a function of the modulation frequency  $\omega$  of (a) linear parametric modulation with  $a_\theta = 0$ ,  $a_\varphi = 0.08$ , and  $(\theta_0, \varphi_0) = (\pi/2, 0)$ ,  $T = 450$  ns; (b) linear parametric modulation with  $a_\theta = a_\varphi = 0.1$ , and  $(\theta_0, \varphi_0) = (\pi/6, 0)$ ,  $T = 400$  ns; (c) elliptical parametric modulation with  $a_\theta = a_\varphi = 0.1$ , and  $(\theta_0, \varphi_0) = (\pi/6, 0)$ ,  $T = 450$  ns.

### G. Precise determination of parametric modulation resonance and oscillation frequency

After preparing the NV center spin in the ground state  $|\psi_0\rangle$  of the Hamiltonian  $\mathcal{H}(\theta_0, \varphi_0)$  by a microwave pulse  $\hat{n}(\varphi_0)|_{\theta_0}$ , we perform parametric modulation resonance measurement by sweeping the parametric modulation frequency  $\omega$ , and measure the probability  $p_0(T)$  that the NV center spin remains in the ground state  $|\psi_g\rangle$ , from which we can roughly determine the resonant frequency. The more accurate we determine the parametric modulation resonant frequency, the more precise we can extract the information on quantum geometry. Therefore, in the experiments, we optimise the parametric modulation frequency to achieve the best possible oscillation contrast in order to improve the accuracy in determining the Rabi frequency. Fig.S4 shows coherent

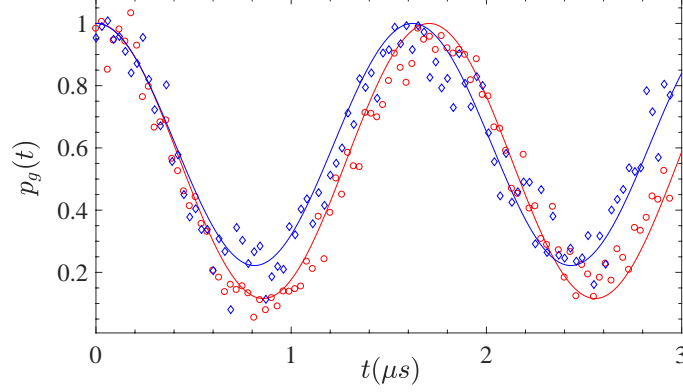


FIG. S4. **Identification of exact resonance frequency.** Coherent oscillation under elliptical parametric modulation with slightly different modulation frequency  $\omega = (2\pi)20.98$  MHz (red,  $\circ$ ) and  $\omega = (2\pi)20.82$  MHz (blue,  $\diamond$ ). The other parameters are:  $\theta_0 = \pi/4$ ,  $\varphi = 0$ ,  $a_\theta = 0.1$  and  $a_\varphi = 0.1$ .

transition from the ground state to the excited state on parametric modulation with slightly different modulation frequency. It can be seen that when the resonant condition is better matched, the parametric modulation induced coherent oscillation demonstrates a higher contrast. We observe that the Rabi frequencies depend on the modulation amplitudes, but also, on the form of the parametric modulation, which is shown to represent direct signatures of the system's quantum geometry..

#### H. Detecting topological transition from measurement of quantum geometry

The topological transition can be detected in our experiment by extending the Hamiltonian into the following form

$$\mathcal{H}(\theta, \varphi) = \frac{A}{2} \begin{pmatrix} \cos \theta + r & \sin \theta e^{-i\varphi} \\ \sin \theta e^{i\varphi} & -\cos \theta - r \end{pmatrix}, \quad (\text{S.44})$$

where  $r$  is a tunable constant that can be realised with an additional frequency detuning. For different value of  $r$ , the QGT of the Hamiltonian (S.44) can be calculated analytically as

$$g_{\theta\theta} = \frac{(1 + r \cos \theta)^2}{4(1 + r^2 + 2r \cos \theta)^2}, \quad (\text{S.45})$$

$$g_{\varphi\varphi} = \frac{\sin^2 \theta}{4(1 + r^2 + 2r \cos \theta)}, \quad (\text{S.46})$$

$$g_{\theta\varphi} = 0, \quad (\text{S.47})$$

$$\mathcal{F}_{\theta\varphi} = \frac{\sin \theta (1 + r \cos \theta)}{2(1 + r^2 + 2r \cos \theta)^{3/2}}. \quad (\text{S.48})$$

With a finite value of  $r$ , all elements of the QGT can also be measured directly in our experiment using the similar method as described in the main text. In this case, the frequency of parametric modulation would depend on  $\theta$  because the eigenenergies of Hamiltonian (S.44) are

$$E_{\pm}(r, \theta, \varphi) = \pm \frac{A}{2} \sqrt{1 + r^2 + 2r \cos \theta}, \quad (\text{S.49})$$

which change with the value of  $\theta$ . The NV center spin shall be initialised into the eigenstate

$$|\psi_g\rangle = \cos \frac{\theta'}{2} |-1\rangle + \sin \frac{\theta'}{2} e^{i\varphi} |0\rangle \quad \text{with} \quad \theta' = \cos^{-1} \frac{\cos \theta + r}{\sqrt{1 + r^2 + 2r \cos \theta}}, \quad (\text{S.50})$$

which depends on the value of  $r$ .

When  $r = 0$ , we can look at the parameter space as a sphere  $S^2$  embedded in  $\mathbb{R}^3$ , with a magnetic (Dirac) monopole at its origin. Changing the additional parameter  $r$  moves the location of this monopole away from the origin, and the topology of this parameter space is characterized by the number of monopoles inside the sphere. The number of monopoles is counted by the Chern number, which is the integral of the Berry curvature over the sphere (7)

$$C = \frac{1}{2\pi} \int_{S^2} \mathcal{F}_{\theta\varphi} d\theta d\varphi. \quad (\text{S.51})$$

For a finite value of  $r$ , the distribution of Berry curvature  $\mathcal{F}_{\theta\varphi}$  is not symmetric on both sides of  $\theta = \pi/2$ . When  $r$  approaches 1, the value of  $\mathcal{F}_{\theta\varphi}$  has a singularity around  $\theta = \pi$  which corresponds to a topological transition, where the monopole moves out of the sphere. In terms of the Chern number, the Chern number is  $C = 1$  when  $r < 1$ , but  $C = 0$  when  $r > 1$ .